JOURNAL OF MATERIALS SCIENCE **34** (1999) 4751–4759

Ductile fracture mechanisms in shielded metal-arc and gas tungsten-arc welds of Type 347 stainless steels

YONG JUN OH, BONG SANG LEE, SANG CHUL KWON, JUN HWA HONG
Reactor Materials Department, Korea Atomic Energy Research Institute, P.O. Box 105 Yusong, Taejon, 305-600, Korea
E-mail: yjoh@nanum.kaeri.re.kr

The ductile fracture behavior of two different welds of Type 347 stainless steel, which are made by SMAW (shielded metal arc welding) and GTAW (gas tungsten arc welding) processes was characterized by *J*-integral testing and microstructural evaluation techniques. Both welds by SMAW and GTAW processes showed significantly low fracture toughness compared with that of the base metal. Metallographic and fractographic examinations revealed that different micromechanisms are operative in the fracture process of the two welds. In the SMAW weld, the fracture was dominated by void initiation and growth at the inclusions that are homogeneously distributed in the matrix. On the other hand, in the GTAW weld, a large number of Nb(CN) particles precipitated on the austenite/ferrite interface as long rod shapes and the fracture proceeded by void initiation at these particles and accompanying decohesion of the interface. It is recommended that the C and Nb contents be reduced in weld metal itself as well and that the welding atmosphere be controlled.

1. Introduction

Niobium stabilized Type 347 austenitic stainless steel (SS) is now widely used as piping material in the nuclear and oil industries for its high corrosion resistance and good strength. The current design concept for nuclear piping is based on the elastic-plastic fracture mechanics technology, such as leak-before-break (LBB) analysis, and additional material properties of fracture toughness are prerequisite to the detailed analysis. Even though the austenitic stainless steels generally exhibit excellent ductility, the fracture toughness of welds may strongly depend on the welding conditions [1–9]. The most important microstructural factors affecting ductile fracture properties of welds may be the inclusions and the retained delta-ferrite since they can cause void initiation and matrix decohesion [10, 11]. Shielded metal arc welding (SMAW) is the most widely used process in the field because of its versatility. But it exhibits some deficiency in cleanliness due to slag formation. Therefore, gas tungsten arc welding (GTAW) is applied wherever the cleanliness of the weld is critical in order to improve the mechanical properties by reducing the amount of inclusions. Landes and McCabe [7] indicated that the fracture toughness of GTAW welds was similar to that of the base metal while the SMAW weld showed significantly lower toughness. Delta-ferrite in welds may also reduce toughness by decreasing ductility [8]. The degradation due to delta-ferrite formation in austenitic stainless steels is, however, thought to be less severe than from inclusions.

Unlike the common Type 304 SS, Type 347 SS contains niobium carbide in the austenite matrix. Niobium is a strong carbide former and added to prevent the preferential formation of chromium carbide that is harmful to the intergranular corrosion resistance. However, the presence of niobium carbide may also reduce fracture resistance. Some investigators showed Type 347 SS has reduced fracture resistance compared to the unstabilized steels due to the presence of niobium carbide [8, 12]. However, reports for the fracture behavior of Type 347 SS weldments are very rare, in spite of the expected harmful effects of the carbides. The objective of the present paper is to characterize the fracture properties of Type 347 stainless steel welds that are made by the two different welding processes, SMAW and GTAW. Special emphasis is focussed on identifying the controlling microstructural factors for fractures and finding possible ways to reduce the detrimental effect on welds.

2. Experimental

2.1. Materials

The chemical compositions of commercial Type 347 SS base metals and weld metals are shown in Table I. The geometry of the weldments and orientation of *J*-*R* test specimens are depicted in Fig. 1. Weld deposition on each pass was controlled at a maximum thickness of 3 mm. Heat-1 and Heat-2 base alloys were welded using GTAW and SMAW processes, respectively. The

TABLE I Chemical compositions of commercial Type 347 stainless steels base and weld metals

Weldments		C	Mn	P	S	Si	Ni	Cr	Nb+Ta	N
SMAW	Base (Heat-1)	0.050	1.65	0.027	0.007	0.46	10.2	17.4	0.67	0.120
	Weld	0.032	1.02	0.029	0.003	0.83	10.0	19.4	0.38	0.055
GTAW	Base (Heat-2)	0.060	1.65	0.022	0.005	0.51	11.1	18.0	0.78	0.120
	Weld	0.047	1.37	0.025	0.015	0.44	9.35	19.2	0.56	0.043

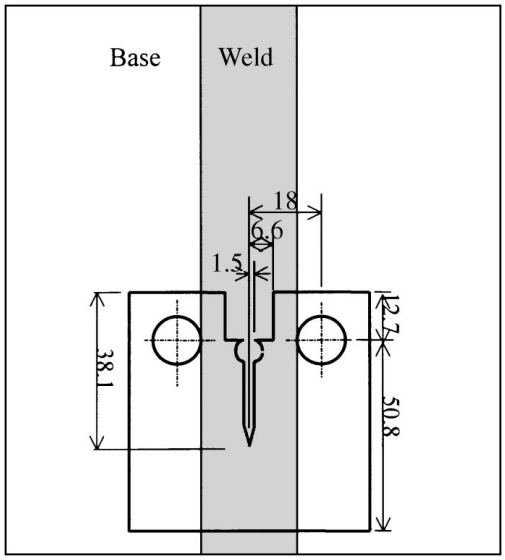

Figure 1 The geometries of the Type 347 SS weldment and the *J*-*R* test specimen (unit: mm).

contents of delta-ferrite in the welds were measured by magnetic permeability with a Magne-gauge instrument.

2.2. Fracture toughness testing

Compact tension specimens (1T-CT) with 1 in. thickness for measuring *J*-integral resistance (*J*-*R*) curves were taken from weldments and they were oriented such that the crack growth proceeded along the weld direction (TL orientation). After pre-cracking, the specimens were side-grooved a total of 20% of the thickness with 45° notch and 0.5 mm root radius. Testing was performed by the unloading compliance *J*-integral test method, in general accordance with ASTM E1737-96, at 316 °C which is the reactor coolant temperature of a nuclear power system.

2.3. Microstructural analysis

In addition to metallographic observation, the microstructures of welds were evaluated by transmission electron microscopy (TEM) using energy dispersive X-ray spectroscopy (EDX). Thin foils were prepared by conventional twin-jet thinning method. Scanning electron microscopy (SEM) was also used for microstructural observation of the etched sample and for the fractographic examination of the *J*-*R* fracture surface.

In order to examine the 3-dimensional features of fracture, the fracture surfaces were sectioned along the crack growth direction and the resulting surfaces were observed after slight etching with an etchant of 20 ml acetic acid, 20 ml nitric acid, 30 ml hydrochloric acid and 10 ml glycerol.

2.4. Simulation of the fracture process

In order to observe the fracture processes in on microscopic scale, small specimens were machined for three

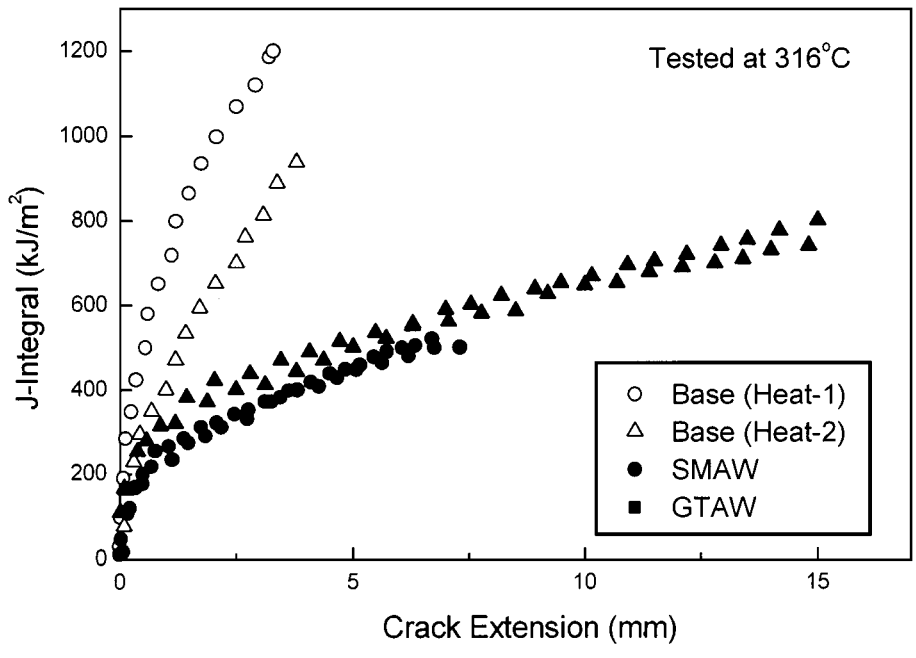

Figure 2 *J*-*R* test results for Type 347 SS base metal (Heats-1, 2) and welds.

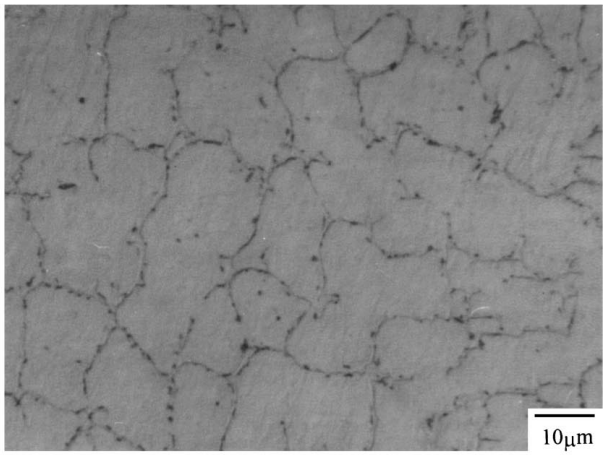

(a)

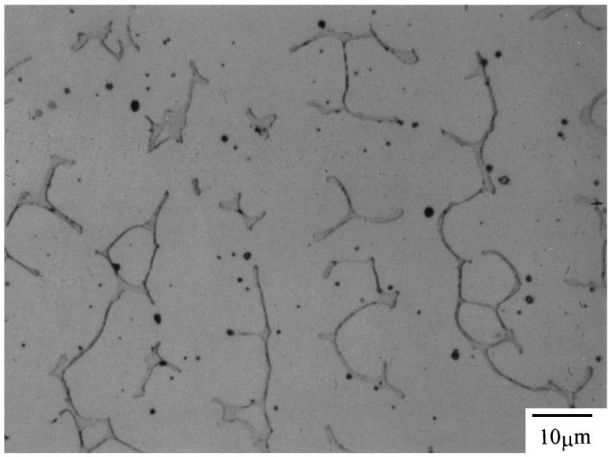

(b)

Figure 3 Optical microstructures of Type 347 SS welds: (a) GTAW and (b) SMAW.

point bend tests in a SEM stage. The size of the specimens was 3.5(W) × 1.3(T) × 12(L) mm and a 1 mm deep notch was cut using a diamond saw. Each side of the specimen surface was carefully polished and etched before bending to reveal the weld structure.

3. Results and discussion

3.1. Tensile and fracture toughness properties

Tensile test results at 316 °C are shown in Table II. Yield strength and tensile strength were higher for the GTAW weld than the SMAW weld but elongation was similar for the two welds.

Fig. 2 summarizes the results of *J*-*R* tests. The results show that the fracture toughness of the welds is significantly lower than that of the base metals, regardless of the applied welding processes. In particular, the GTAW welds exhibit similar low fracture toughness to those

TABLE II Tensile properties at 316 °C of the investigated welds

	YS (MPa)	UTS (MPa)	El. (%)
GTAW	486.4	525.7	18.5
SMAW	310.0	478.0	21.5

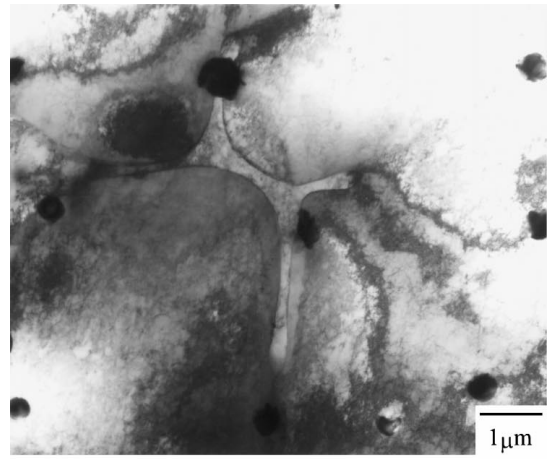

(a)

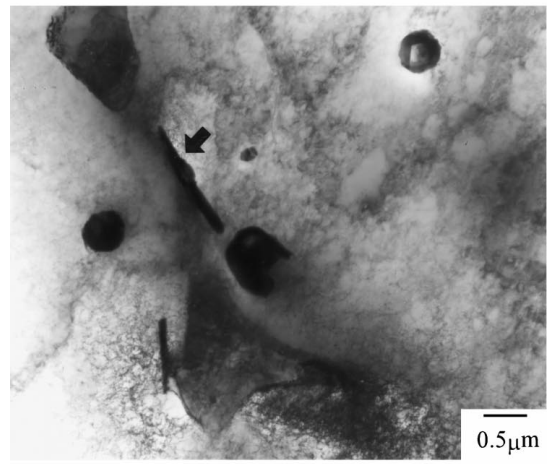

(b)

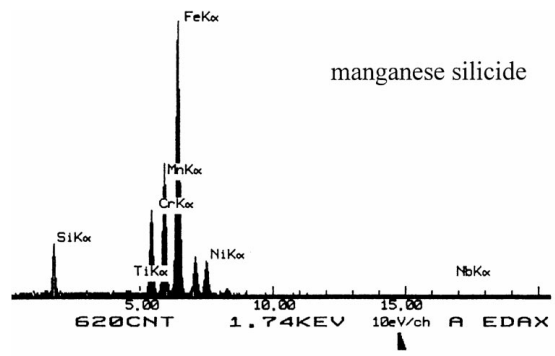

(c)

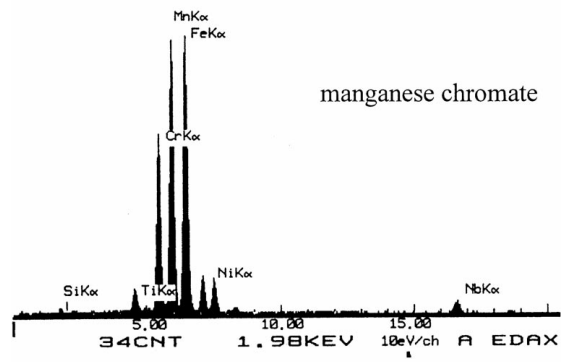

(d)

Figure 4 TEM microstructures of an SMAW weld and EDXS results for the inclusions: (a) inclusions, (b) NbC particles at δ/γ interface (arrows), and (c) and (d) EDX for manganese silicide and manganese chromate, respectively.

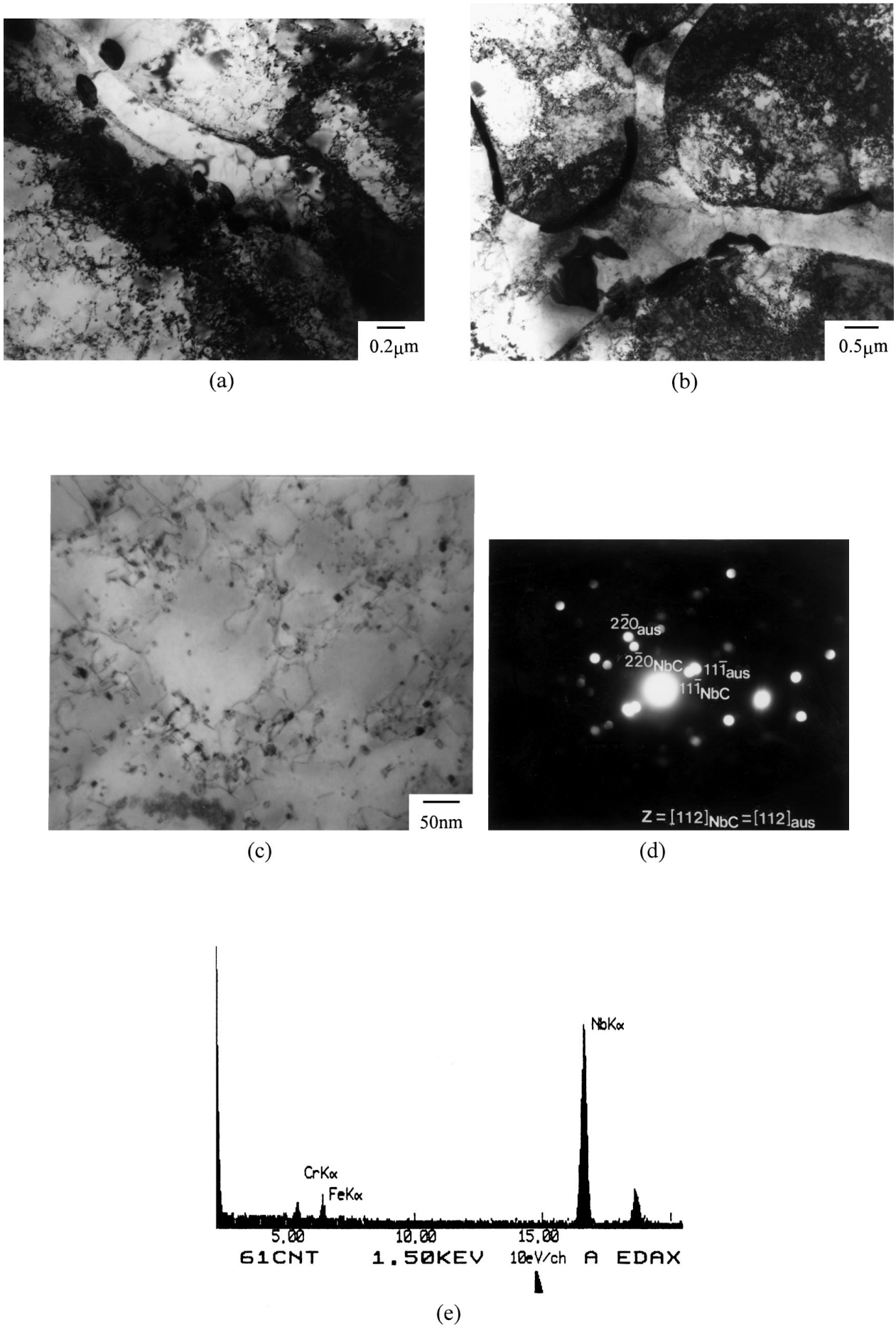

Figure 5 TEM microstructure for GTAW weld: (a) round NbC, (b) rod shaped NbC particles along austenite/ferrite interface, (c) fine NbC particles in the matrix, (d) [112] micro-diffraction pattern and (e) TEM-EDXS results from the fine particle.

using SMAW, indicating that the application of the GTAW process is not enough to improve the toughness of Type 347 SS welds.

3.2. Weld microstructures

Fig. 3 shows optical micrographs of the GTAW and SMAW welds, revealing residual ferrite of approximate width of 1 μm in austenite matrix. The average ferrite contents were found to be 7.5% in the GTAW weld and 5.8% in the SMAW weld, as measured with a Magne-Gage. This difference may have resulted from the higher cooling rate in the GTAW process. A higher cooling rate prevents the primary delta ferrite from transforming to austenite during cooling [13, 14]. In addition, the Cr/Ni equivalent ratio (Cr_{eq}/Ni_{eq}) in the weld wire can influence the amount of delta ferrite [14–16]. However, the difference in Cr_{eq}/Ni_{eq} values between the two welds is small ($Cr_{eq}/Ni_{eq} = 1.80$(SMAW), 1.84(GTAW)), and its effect on the amount of the delta ferrite is expected to be quite small.

In the SMAW weld, large round particles were homogeneously distributed throughout the weld. In the GTAW weld, there were no such large round particles. Instead, small particles with rod shapes were observed along the austenite/ferrite interface in optical micrographs. These were also observed in the SMAW weld, but in quite small amounts.

More detailed information on these particles could be revealed by analytical TEM observation as shown in Fig. 4 through Fig. 7.

Fig. 4 shows the TEM micrographs for the SMAW weld. From the EDX analysis, the large round particles in the SMAW welds was identified as inclusions of two different types. EDX results of Fig. 4c and d indicate those inclusions are manganese silicide and manganese chromate, respectively. Unfortunately, it was nearly impossible to differentiate the two types by the appearance of the inclusions. However, manganese chromate inclusions were more prevalent in population and larger in size than the silicide type. It is interesting that manganese chromate contained Nb as shown in Fig. 4d.

Fig. 5 shows the TEM micrographs in the GTAW weld. The precipitates are observed in both the austenite (γ) and ferrite (δ) matrices and also along the γ/δ interface. The EDX analysis illustrates that most of precipitates are niobium carbide (or carbonitride) as shown in Fig. 5e. The observed NbC particles could be divided into three categories according to their shapes and sizes. The first is a round or square shape of medium size ($\sim$0.5 μm) as shown in Fig. 5a. Most of these were observed at or near γ/δ interfaces. The second is a long rod or plate shaped particle along the γ/δ interface. These particles were most common of the three types. Fig. 5b shows examples of the long rod shaped NbC particles surrounding a ferrite region. But, some of these particles were also observed in the austenite matrix. The third is a small particle which is distributed in the austenite matrix as shown in Fig. 5c. These particles were mainly observed at dislocations in austenite. Similar to those in the base metal [17, 18], these NbC particles showed a bimodal size distribution that is composed of medium size particles and very fine particles($\sim$10 nm).

The crystallographic relationship of NbC particles with the austenite matrix in the base metal is known to have a cube-on-cube relationship [17]:

$$(1\,0\,0)_{NbC}//(1\,0\,0)_{Austenite}$$

$$(1\,1\,1)_{NbC}//(1\,1\,1)_{Austenite}$$

In the welds, the above relationship was also valid for the small intragranular particles as shown in Fig. 5c and for some of the round- or wedge-shape particles of medium size, as shown in Fig. 5a. Fig. 5d provides a typical micro-diffraction pattern showing the above relationship. However, it should be noted that most of the medium and coarse particles at the γ/δ interface, in general, did not have any special crystallographic relationships with either the austenite or the ferrite. Unlike in the SMAW case, there were no large inclusions in the GTAW weld. This is consistent with observations of the optical microstructure.

The NbC particles were also observed in the SMAW weld. Fig. 4b shows the NbC particles at the interface. The number of the particles in the SMAW weld was, however, considerably lower than in the GTAW weld. This is attributed to the use of welding wire with relatively lower Nb and C contents. Nb trapping by inclusions as shown in Fig. 4c is also expected to reduce the number of NbC particles.

A large portion of the γ/δ interfaces linked to NbC particles migrated inward as shown in Fig. 6. Some large rod shaped NbC particles were observed in the austenite matrix. From these, it is inferred that some part of the interfacial NbC particles precipitated before ferrite shrinkage was completed and the shrinkage of ferrite during cooling was interfered by the NbC particles. However, at this time, it is not certain whether the restraining of NbC is effective on the shrinkage of ferrite.

3.3. Fracture processes of the welds

The welds of Type 347 stainless steel exhibited significantly low fracture toughness compared with the base metal, irrespective of the applied welding processes.

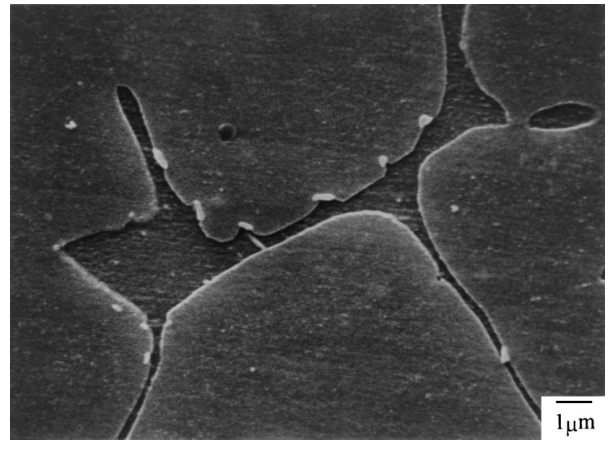

Figure 6 SEM micrograph showing the distortion of the δ/γ interface at the NbC particles during shrinkage of the δ phase. δ/γ interfaces bow between NbC particles.

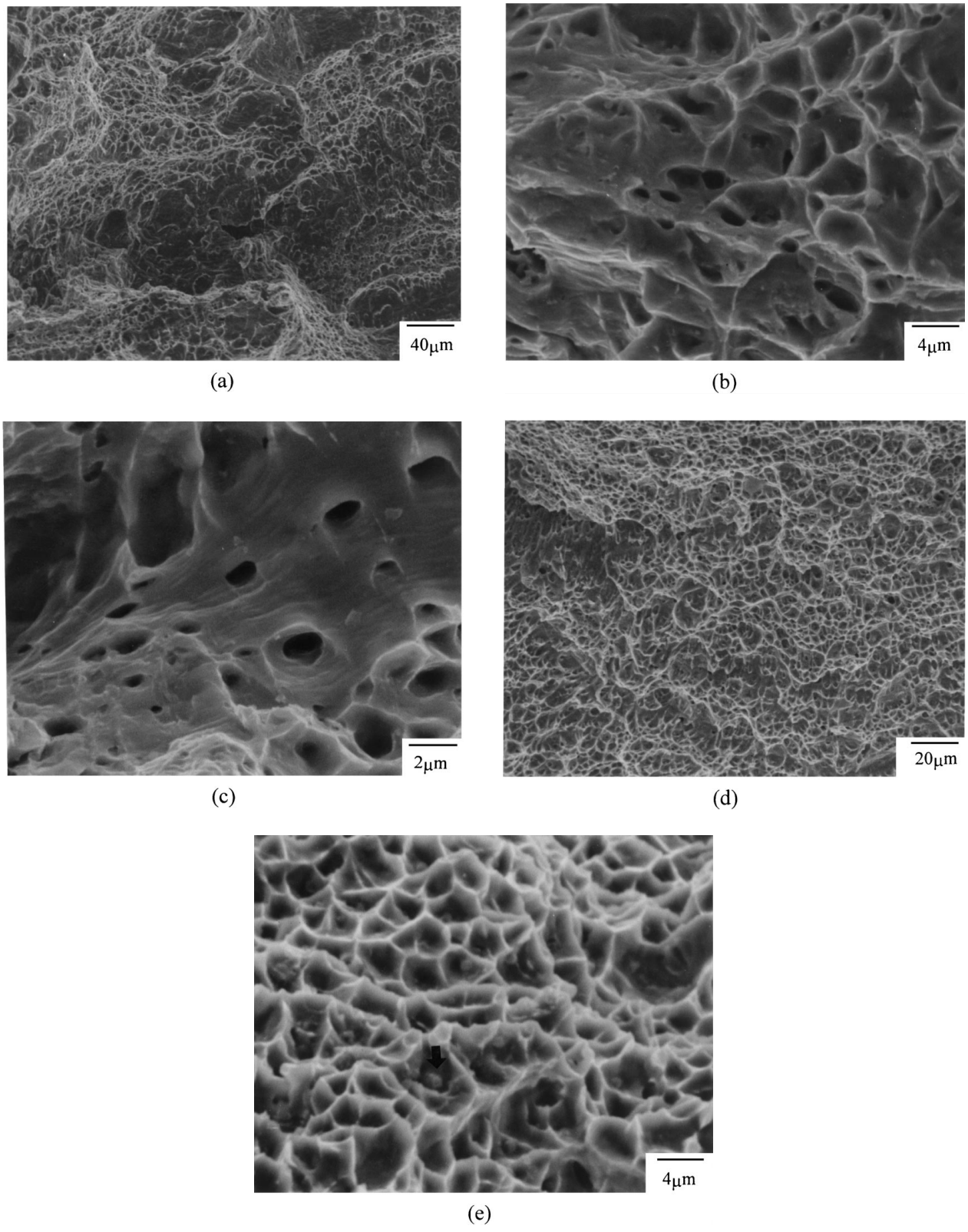

Figure 7 *J-R* fracture surface of GTAW and SMAW welds: (a), (b) and (c) GTAW weld; (d) and (e) SMAW weld (Arrow indicates an inclusion at the center of the dimple).

This means that the cleaner GTAW process did not result in a noticeable improvement in toughness compared to the SMAW process. The reasons for low fracture resistance were investigated by examining the fracture processes in two welds.

The typical appearances of *J-R* fracture surfaces are compared in Figs 7 and 8. On both fracture surfaces, characteristic differences between the GTAW and SMAW welds could be clearly observed both on macroscopic and microscopic scales.

Macroscopically, the fracture surface of the GTAW weld consisted of fine dimpled regions and the larger ductile sheared regions covering about a quarter of the surface as shown in Fig. 7a. Most of the sheared regions were inclined away from the main crack propagation direction. At some locations, deep large cracks were

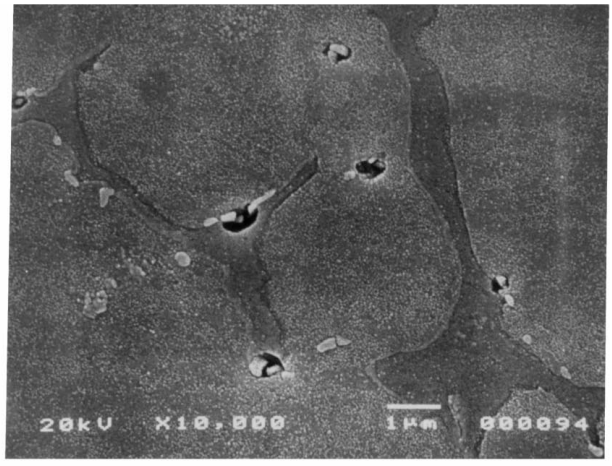

(a)

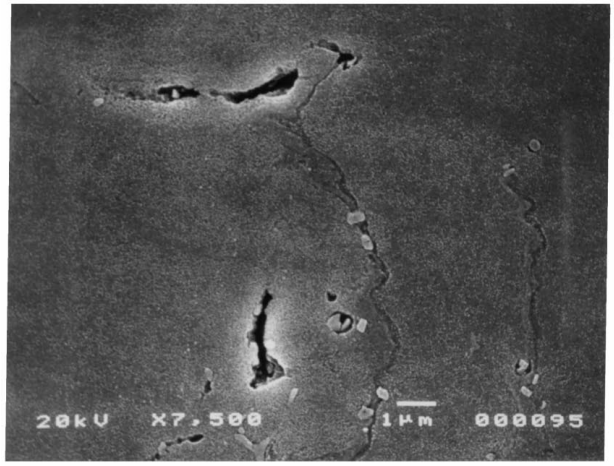

(b)

Figure 8 SEM micrographs of areas beneath the J-R fracture surface of the GTAW weld; SEM microstructures showing initiation (a) and growth (b) of voids at the NbC particles along δ/γ interfaces.

developed. On the other hand, the SMAW weld fracture surface shown in Fig. 7d was mostly covered with ductile dimples without sheared regions. The dimples in the SMAW weld fracture surface were more evenly distributed than for GTAW weld which exhibited a large variation in size. Microscopically, it was observed that most of the dimples in the GTAW weld were shallow, but deep micro-cracks or voids developed in the dimples as shown in Fig. 7b. Some NbC particles were observed in the shallow dimples. The deep micro-voids were also clearly developed in the sheared regions as shown in Fig. 7c. On the SMAW weld fracture surface, however, the number of the deep micro-voids was much lower than that in the GTAW weld case as shown in Fig. 7e. Round large inclusions were observed at the center of the dimples in SMAW.

To observe the microscopic fractures under the fracture surface, sections parallel to the crack propagation direction and loading direction were examined using SEM. Fig. 8 shows micro-cracks or voids beneath the fracture surface in the GTAW weld. The voids initiated at NbC particles at the γ/δ interface. Fig. 8b shows that voids are linked along the interface. This fracture process was also illustrated by the simulated fracture test using a notched three point bend specimen. Fig. 9 shows

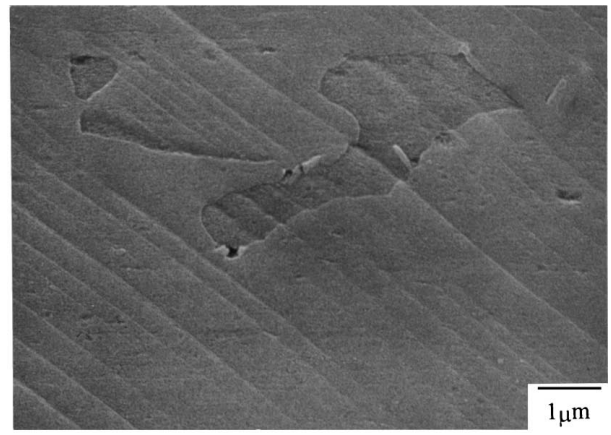

(a)

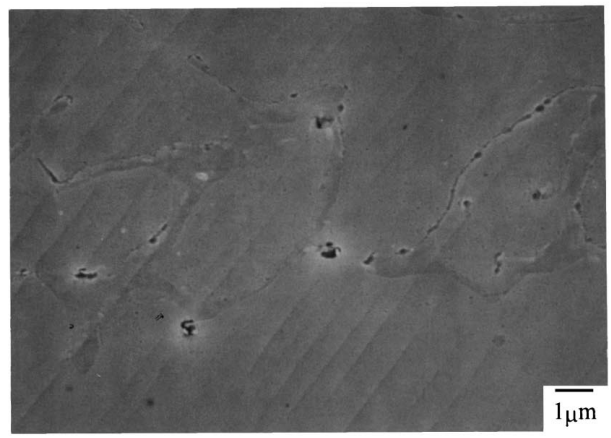

(b)

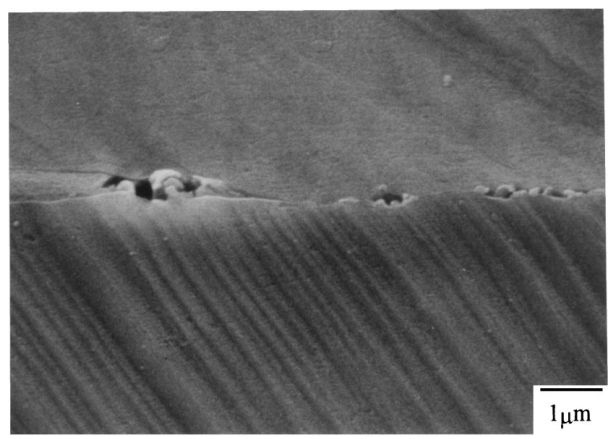

(c)

Figure 9 Simulation of the fracture using a miniaturized 3-point bent test: (a), (b) and (c), showing regions 200, 100, and 50 μm away from the notch-tip respectively.

the microstructure ahead of the crack-tip after bending. Slip lines were developed in the austenite matrix and the voids were initiated at the interface NbC particles impinging against intensive slip lines. At a short distance from the crack-tip, slip lines are closer to each other and the voids at the interface are larger as shown in Fig. 10b and c. However, when the particles were absent at the interface, slip bands in the austenite extended into the adjacent austenite matrix without decohesion of the interface. Accordingly, the fracture of the GTAW

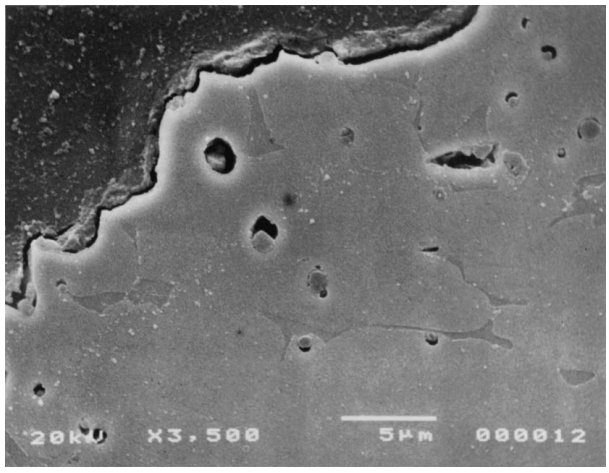

Figure 10 SEM micrograph for an area beneath the *J*-*R* fracture surface of the SMAW weld; Voids are initiated at the round inclusions.

weld arises from crack initiation at NbC particle at the interface and the resulting decohesion of the interface.

On the other hand, the fracture of the SMAW weld proceeded by decohesion of inclusions and matrix. Fig. 10 shows the decohesion at inclusions. The inclusions were uniformly distributed in austenite and ferrite as already shown in Fig. 4. Therefore, the growth of the voids continued without any contribution from the γ/δ interface. The uniform distribution of ductile dimples on the final ruptured surface also supports this fracture process.

The fracture processes for the two welds are schematically depicted in Fig. 11. For the GTAW weld, the micro-voids are initiated by decohesion of the interface as shown in Fig. 11a. Subsequent growth proceeds by the plastic flow of surrounding ductile matrix. The initiated cracks (or voids) normal to the applied stress enlarge by the opening of the crack face along the γ/δ interface, and final fracture is completed with the formation of shallow dimples on the fracture surface. On the other hand, the cracks (or voids) at the interface parallel to the loading axis grow into ellipsoidal shapes parallel to the loading axis. This type of voidage can also contribute to deteriorating fracture resistance by reducing effective ligaments between coalescing large voids, even though they do not grow to large voids that are linked to final dimples. However, in the SMAW weld, as shown in Fig. 11b, the void initiation and growth at the inclusions, which are uniformly distributed in matrix, control the entire fracture process and result in a large number of elongated cusps and deep dimples, exhibiting the inclusions at their centers.

As a result, the low fracture resistance of the GTAW weld was mainly attributed to the NbC particles at austenite/ferrite interface. The formation of NbC particles in Type 347 stainless steel weld is thought to be unavoidable, because the solubility of Nb in Type 347

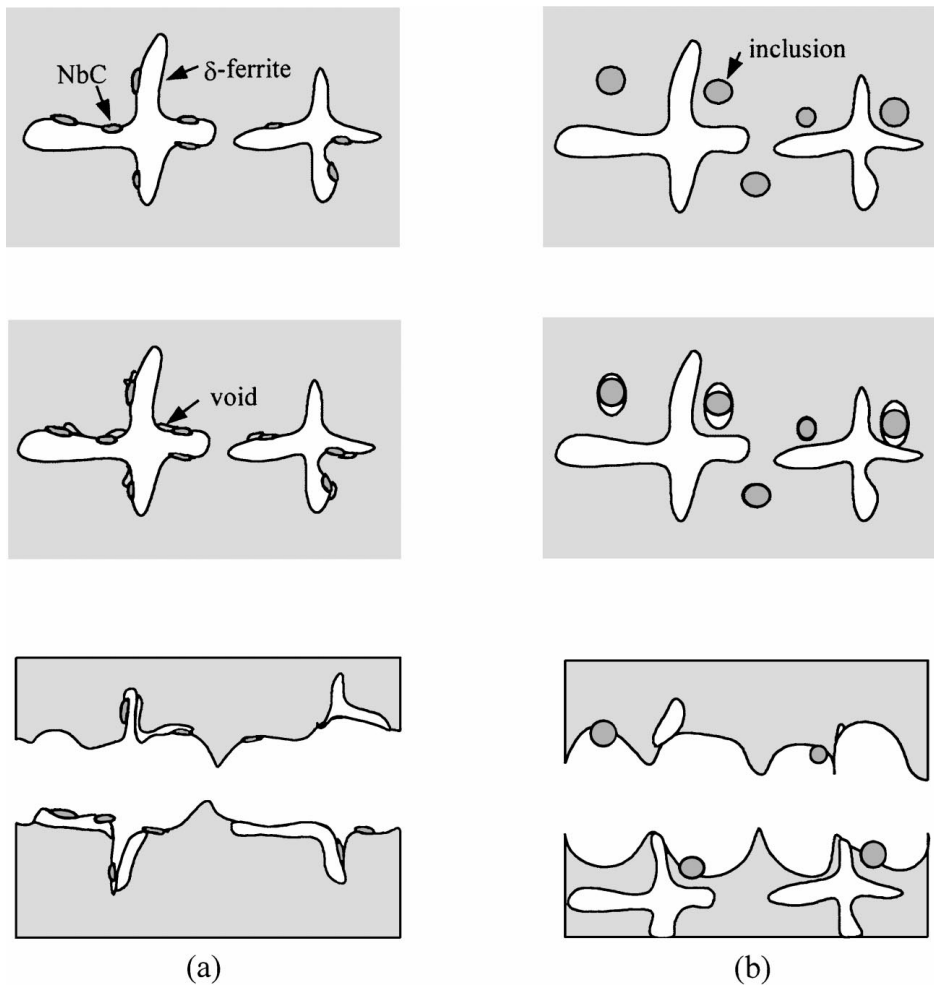

Figure 11 Schematic representation of fracture processes in GTAW (a) and SMAW (b).

is very low even at a high temperature [12, 19]. Accordingly, in order to improve the fracture resistance of the weld, it is recommended that Nb and C contents in welding wire should be reduced enough to repress the long rod shape of particles at the γ/δ interface, in addition to the high cleanliness of the weld.

4. Conclusions

The results of this investigation for Type 347 stainless steel welds, which were made by SMAW and GTAW processes, allow the following conclusions:

(1) J-integral fracture tests of two welds at 316 °C resulted in dramatically reduced ductile fracture resistance properties in comparison with those of the base metals. The commercial GTAW weld of high cleanliness also exhibited very low fracture toughness similar to the SMAW weld.

(2) In the GTAW weld, a large number of NbC particles were precipitated to show a bimodal size distribution that is composed of fine and coarse particles. The coarse particles precipitated mainly along the austenite/ferrite interface as a long rod shape while the fine precipitates were rather homogeneously distributed in the matrix. The fracture was controlled by the coarse NbC particles where the voidage was initiated and linked along the austenite/ferrite interface without extensive plastic deformation. The austenite/ferrite interface with NbC particles was an effective crack growth path while those without NbC particles were resistant to fracture.

(3) In the SMAW weld, relatively large inclusions were homogeneously distributed in the matrix. These inclusions were found to be manganese chromate and manganese silicide that may have originated from the low cleanliness of the welding process. However, the number of NbC particles was small due to the reduced contents of Nb and C in the weld wire. Therefore, the fracture was conventionally controlled by void initiation and growth at the large inclusions.

The low fracture resistance of GTAW welds is therefore attributed to the large NbC particles at the austenite/ferrite interface while the metallic inclusions were limited by controlling the welding atmosphere. Because NbC formation during solidification in Type 347 stainless steel welds seems to be unavoidable, in order to improve fracture resistance, it is recommended that the C and Nb contents be reduced in the weld metal itself besides controlling the welding atmosphere.

Acknowledgements

This work is a part of the Reactor Pressure Boundary Materials Project, which has been financially supported by the Korea Ministry of Science and Technology.

References

1. W. J. MILLS, *Eng. Fracture Mechanics* **30** (1988) 469.
2. W. H. BAMFORD and A. J. BUSH, *ASTM STP* **668** (1979) 553.
3. M. F. KANNINEN, A. ZAHOOR, G. WILKOWSKI, I. ABOU-SAYED, C. MARSHALL, D. BROAK, S. SAMPATH, H. RHEE and J. AHMAD, EPRI NP-2347, Battelle Columbus Laboratories, Columbus, OH, 1982.
4. G. M. WILKOWSKI, A. ZAHOOR and M. F. KANNINEN, *J. Press. Vess. Technol.* **103** (1981) 359.
5. C. G. CHIPPERFIELD, *Int. J. Fracture* **12** (1976) 873.
6. K. YOSHIDA, M. KOJIMA, M. IIDA and I. TAKAHASHI, *Int. J. Pres. Ves. and Piping* **43** (1990) 273.
7. J. D. LANDES and D. F. MCCABE, *EPRI NP-4768* (1986).
8. P. BALLADON and J. HERITIER, *ASTM STP 905* (1986) 661.
9. C. G. CHIPPERFIELD, *I. Mech. Eng.* (1978) 145.
10. P. BALLADON, J. HERITIER and P. RABBE, *ASTM STP 791* (1983) II-496.
11. T. C. MILLER and T. L. ANDERSON, *ASTM STP 1207* (1994) 87.
12. T. P. MAGEE and HOFFMANN, *ASME* (1995) 267.
13. N. SUUTALA, T. TAKALO and T. MOISIO, *Metall. Trans.* **11A** (1980) 717.
14. J. A. BROOKS, J. C. WILLIAMS and A. W. TOMPSON, *ibid.* **14A** (1983) 23.
15. O. HAMMER and U. SVENSSON, "Solidification and Casting of Metals" (Metal Society, London, 1979) p. 362s.
16. Y. SONG, T. N. BAKER and N. A. MCPHERSON, *Mater. Sci. Eng.* **A212** (1996) 228.
17. W. J. LIU and J. J. JONAS, *Metall. Trans.* **19A** (1988) 1415.
18. J. M. SILCOCK, *Acta Metall.* **14** (1966) 687.
19. R. AYER, C. F. KLEIN and C. N. MARZINSKY, *Metall. Trans.* **23A** (1992) 2455.
20. M. ERVE, U. WESSLING, R. KILIAN, R. HARDT, G. BRUMMER, V. MAIER and U. ILG, *Nucl. Eng. and Design* **171** (1997) 113.
21. J. R. RICE and D. M. TRACEY, *J. of the Mechanics and Physics of Solid* **17** (1969) 201.

Received 30 July 1998
and accepted 26 March 1999